A Rapid and Low-cost Fabrication and Integration Scheme to Render 3D Microfluidic Architectures for Wearable Biofluid Sampling, Manipulation, and Sensing

Complete List of Authors:	Lin, Haisong; University of California Los Angeles, Electrical and Computer Engineering Zhao, Yichao; University of California Los Angeles, Materials Science and Engineering Lin, Shuyu; University of California Los Angeles, Electrical and Computer Engineering Wang, Bo; University of California Los Angeles, Electrical and Computer Engineering Yeung, Christopher; University of California Los Angeles, Materials Science and Engineering Cheng, Xuanbing; University of California Los Angeles, Materials Science and Engineering Wang, Zhaoqing; University of California Los Angeles, Electrical and Computer Engineering Cai, Tianyou; University of California Los Angeles, Electrical and Computer Engineering Yu, Wenzhuo; University of California Los Angeles, Electrical and Computer Engineering King, Kimber; University of California Los Angeles, Electrical and Computer Engineering Tan, Jiawei; University of California Los Angeles, Materials Science and Engineering Salahi, Kamyar; University of California Los Angeles, Electrical and Computer Engineering Hojaiji, Hannaneh; University of California Los Angeles Henry Samueli School of Engineering and Applied Science, Electrical and Computer Engineering Emaminejad, Sam; University of California Los Angeles, Electrical and Computer Engineering

SCHOLARONE™
Manuscripts

A Rapid and Low-cost Fabrication and Integration Scheme to Render 3D Microfluidic Architectures for Wearable Biofluid Sampling, Manipulation, and Sensing

Haisong Lin[1], Yichao Zhao[1,2], Shuyu Lin[1], Bo Wang[1], Christopher Yeung[1,2], Xuanbing Cheng[1,2], Zhaoqing Wang[1], Tianyou Cai[1], Wenzhuo Yu[1], Kimber King[1], Jiawei Tan[1,2], Kamyar Salahi[1], Hannaneh Hojaiji[1], and Sam Emaminejad[1*]

[1] Department of Electrical and Computer Engineering, University of California, Los Angeles, CA, USA

[2] Department of Materials Science and Engineering, University of California, Los Angeles, CA, USA

* Correspondence and requests for materials should be addressed to S.E. (emaminejad@ucla.edu)

Abstract

The large-scale deployment of wearable bioanalytical devices for general population longitudinal monitoring necessitates rapid and high throughput manufacturing-amenable fabrication schemes that render disposable, low-cost, and mechanically flexible microfluidic modules capable of performing a variety of bioanalytical operations within a compact footprint. The spatial constraints of previously reported wearable bioanalytical devices (with microfluidic operations confined to 2D), their lack of biofluid manipulation capability, and the complex and low-throughput nature of their fabrication process, inherently limit the diversity and frequency of end-point assessments, and prevents their deployment at large scale. Here, we devise a simple, scalable, and low-cost "CAD-to-3D Device" fabrication and integration scheme, which renders 3D and complex microfluidic architectures capable of performing biofluid sampling, manipulation, and sensing. The devised scheme is based on laser-cutting of tape-based substrates, which can be programmed at the software-level to rapidly define microfluidic features such as biofluid collection interface, microchannels, and VIAs (vertical interconnect access), followed by the vertical assembly of pre-patterned layers to realize the final device. To inform the utility of our fabrication scheme, we demonstrated three representative devices to perform sweat collection (with visualizable secretion profile), sample filtration, and simultaneous biofluid actuation and sensing (using a sandwiched-interface). Our devised scheme can be adapted for the fabrication and manufacturing of current and future wearable bioanalytical devices, which in turn will catalyze the large-scale production and deployment of such devices for general population health monitoring.

Introduction

In recent years, the maturity and convergence of the fields of electrochemistry, flexible device fabrication, and low-power electronics have led to the development of wearable biomarker sensors that can probe non-invasively-retrievable biofluids, such as sweat, to measure the concentration of physiologically informative biomarker molecules [1-6]. Accordingly, electrochemical [7-10] and colorimetric sensors [11-14], based on enzymatic, ion-selective, and electroactive interfaces have been developed to target analytes such as metabolites and electrolytes. To facilitate robust analytical operations, wearable bioanalytical devices utilize mechanically flexible microfluidic housings to collect and analyze the biofluid samples, while minimizing sample evaporation and external contamination [15-17].

Numerous device fabrication-related criteria including scalability, cost-effectiveness, flexibility, compactness, and ease-of-integration are yet to be addressed to catalyze the large-scale deployment of demonstrated and envisioned bioanalytical devices for general population monitoring [18-20]. Specifically, high throughput manufacturing-amenable fabrication schemes are required to render low-cost and skin-conformal microfluidic modules. That is because, to eliminate the fundamental challenges such as contamination (from residues of old samples) and sensor biofouling, the microfluidic modules are implemented as disposable units, which are to be replaced frequently to perform longitudinal monitoring. Furthermore, the fabrication scheme must be capable of rapidly realizing and integrating a variety of bioanalytical components, including biofluid manipulation, actuation, and sensing interfaces within a compact footprint to allow for the quantification of a panel biomarkers, which is key to providing a comprehensive view of the user's physiological state. The majority of reported wearable bioanalytical device implementations rely

on conventional Polydimethylsiloxane (PDMS)-based soft-lithography methods [9, 11, 12, 15], which require access to resource-intensive facilities for device fabrication and assembly. Specifically, for such approaches, the mold is fabricated in nanofabrication and cleanroom facilities, following time-consuming and multi-step protocols, with designs that are fixed by corresponding mask designs, which often need to be separately custom-ordered and purchased from third-party vendors (for each design) [21, 22]. Additionally, the device assembly requires surface activation by oxygen plasma treatment, which provides a short time-window for alignment and bonding. Furthermore, the reported wearable biomarker sensors relied on the analysis of the sample biofluid, collected in 2D microfluidic devices [9, 11, 12, 15]. The spatial constraints of these sensors inherently limits the versatility and quantity of bioanalytical operations, consequently constraining the diversity and frequency of end-point assessments.

To address these limitations, we devise a simple, scalable, and low-cost "CAD-to-3D Device" fabrication and integration scheme, which renders 3D, flexible, and complex microfluidic architectures. The devised scheme is based on laser-cutting and vertical assembly of thin layers of tape-based substrates. The laser-cutter can be programmed at the software-level to rapidly define microfluidic features such as biofluid collection interface, microchannels, and VIAs (vertical interconnect access), with different dimensions. By leveraging the adhesive property of the substrates and elaborate positioning of microfluidic VIAs, the 2D-patterned layers can simply be stacked and fluidically routed to form leakage-free, multilayered, and 3D architectures. Furthermore, to deliver a diverse set of operations, as part of the devised scheme, electrode-patterned layers can be incorporated during the assembly process to facilitate actuation and sensing functionalities.

The devised fabrication and integration scheme can be adapted to implement a diverse set of bioanalytical operations. To illustrate this point, we demonstrated three representative devices to perform sweat collection (with visualizable secretion profile), sample filtration, and simultaneous biofluid actuation and sensing (using a sandwiched interface). To demonstrate the reliable and leakage-free epidermal sweat sampling capability, a flexible and adhesive sweat collector interface is designed that can simply attach to the skin as a standalone unit. The interface is based on a microfluidic epidermal configuration, which harvests sweat, with minimized dead volume, and uses a fluidic VIA to route the collected sample through a microfluidic channel with the planar Archimedean Spiral design. This configuration allows for the visualizing the sweat secretion profile and inferring the secretion rate through optical imaging. Furthermore, to illustrate the value of the devised scheme to render complex and 3D functional architectures, we demonstrate a flyover architecture, based on a network of over/under-pass microchannels, capable of performing multi-step size-based μ-scale filtration in z-axis, with the aid of vertically-integrated-filtration embodiments (incorporated during the device assembly). In the context of wearable biomarker sensing, μ-scale filtration may be adapted to eliminate contamination arising from epidermis or to perform other bioanalytical operations (similar to those shown in lab-on-a-chip settings) [23-26]. Finally, to illustrate the enabling multi-functional operations achievable by the devised scheme, we present a sandwiched-like interface, which incorporates electrode-patterned layers to perform simultaneous actuation and sensing within a microfluidic channel. As an example, we demonstrate simultaneous AC electrothermal actuation (ACET, with electrode pair on the ceiling) and electrochemical analysis (amperometric sensing, with electrode array on the bottom). The results show that the activation of ACET enhances the sensitivity and reduces the response time of the amperometric sensors.

Materials and method

Fabrication and assembly of wearable microfluidic modules

The microfluidic modules were created by assembling several layers of double-sided tape (170 μm-thick, 9474LE 300LSE, 3M) and transparent PET film sheets (100 μm-thick, MG Chemicals, which were selectively patterned with actuation and sensing electrodes). Skin adhesive medical tape (Tegaderm Transparent Film Dressing, 3M) can be incorporated in the assembly process to form the skin-interfacing layer. The microfluidic embodiments, including microchannels and VIAs, were created by laser-cutting (Epilog Mini 24, Epilog Laser) 2D patterns within the tape- and the PET-based substrates. The minimum resolution of the microfluidic device depends on the resolution of the laser-cutter. Using our basic laser cutter, we could achieve ~100 μm features. A more advanced laser cutter can be used, if higher resolution is needed, which can render features with resolution on the order of ~10 μm. With the proper alignment of VIAs and microchannels, fluidic connections in vertical direction were achieved, rendering the complex 3D microfluidic structures. Here, the electrode arrays were patterned on PET substrates by photolithography using positive photoresist (MicroChemicals AZ5214E), followed by the evaporation of 20 nm Cr, 100 nm Au, and 20 nm Ti for actuation electrodes and 20 nm Cr and 100 nm Au for sensing electrodes. After deposition, the lift-off step was performed in acetone. For the envisioned low-cost and disposable device design applications, screen-printing techniques can be used to pattern electrodes (following well-established protocols [27]).

Sweat rate characterization

To conduct the sweat rate measurement test, first, the volar surface of the forearm of the subject was cleaned with Isopropyl alcohol (IPA, Thermo Fisher Scientific Inc, USA), then stimulated with iontophoresis (ITP, ELITechGroup, France) to induce sweat following the standard protocol [27]. Next, as described in the Results and discussion section, the sweat collector was securely placed on the stimulated area. The complete process of sweat filling the spiral channel was video-recorded. The real-time volume of the secreted sweat in the channel was determined based on the designed geometry (Archimedean Spiral:$r = a + b\theta$, where r and θ are polar coordinates, and $a = 1.1\ mm$ and $b = \frac{1}{\pi}\ mm$, as per our design) [28]. Sweat rate information can be inferred by calculating the slope of the sweat volume *vs.* time curve at the desired time-point.

Assembly of vertically-integrated microscale filtering device

Filter papers with different pore sizes (8 um and 30 um, GE Healthcare Life Sciences, USA) were used to remove microbeads (Diameter: 90 um and 10 um, concentration: 2.2×10^3 beads/mL and 1.6×10^6 beads/mL, Polybead, USA) within the biofluid stream in a step-by-step manner. Filter papers were laser-cut into circles and embedded within the designated VIAs. Two layers of double-sided tape were used to seal the filter paper and ensure that all incoming biofluid passed through the filter paper without leakage. Microscopic images of three channel layers were taken to show the significant reduction of beads before and after two cycles of filtration.

Amperometric sensor development and characterization

To develop the hydrogen peroxide (H_2O_2) sensor, a Prussian blue (PB) mediator layer was deposited onto the Au-patterned electrodes (1 mm^2) by cyclic voltammetry from 0 to 0.5 V (*vs.*

Ag/AgCl) for one cycle at a scan rate of 20 mV/s in a fresh solution containing 2.5 mM FeCl$_3$, 100 mM KCl, 2.5 mM K$_3$[Fe(CN)$_6$], and 100 mM HCl. Then, a 1 wt% chitosan solution (Sigma-Aldrich, USA) was prepared by dissolving chitosan in a 2 wt% acetic acid (Sigma-Aldrich, USA) and stirring for 30 min. By drop-casting a 0.5 μL chitosan solution onto Au/PB electrode, the H$_2$O$_2$ sensing interface was realized. To create the glucose sensor, the 1% chitosan solution was mixed thoroughly with a glucose oxidase solution (50 mg/mL in PBS, pH 7.2, Sigma-Aldrich, USA) at a 1:1 ratio (volume/volume). By drop-casting 1 μL of the mixture onto the Au/PB electrode, the glucose sensing interface was realized. To create the choline sensor, a 0.5 μL choline oxidase solution (0.5 unit/μL in DI water, pH 7.2, Sigma-Aldrich, USA) was placed onto the Au/PB electrode, dried at room temperature, and drop-casted with the of 0.5 μL 1% chitosan solution. The sensors were dried overnight at 4 °C, while protected from light. The sensors were stored at 4 °C when not in use. For all amperometric sensors, the reference/counter electrodes were fabricated by additionally depositing Ag/AgCl ink (Ercon) and heating the electrodes at 80 °C for 10 min.

To characterize the developed sensing interfaces, constant potential amperometric measurements were conducted in PBS buffer (pH = 7.2) at -0.1 V *vs.* Ag/AgCl. The chronoamperometric response was recorded by a potentiostat (CH Instruments) for 60 s. Calibration plots were obtained by introducing different concentrations of the targets (*e.g.*, H$_2$O$_2$, glucose, and choline) in the PBS buffer. Accordingly, the limit of detection (LOD) for each amperometric sensing interface was calculated as LOD$_{glucose}$: 17.6 μM, LOD$_{choline}$: 7.2 μM, and LOD$_{H2O2}$: 3.9 μM (LOD = 3SD/slope, where SD is the standard deviation of the baseline noise in blank solution). These characterization results indicate that the electrochemical sensing interfaces have similar performance as that previously reported by us and others ([7,8], which is as expected, since similar sensor fabrication protocol was followed as those previously reported). In that regard,

given that our sensors and those referenced are all Prussian Blue-based, our sensors present similar benefits (*e.g.*, lowering the excitation voltage, which mitigates the electroactive species' interference) and drawbacks (*e.g.*, generally suffering from oxygen fluctuation) as those sensors.

To characterize the ACET actuation-enhanced sensor response, we used the sandwiched-electrode interface containing the actuation and sensing electrodes (as described in the main text). The ACET actuation electrodes were powered by a function generator (Tektronix, AFG3102C). To compare the effects of ACET actuation on the sensor response, first, the calibration plot for the case of no ACET actuation was obtained, as described before. Then, the calibration plot of the sensor in presence of ACET actuation was obtained by applying 3.5 V_{RMS} (10 MHz) across the ACET electrodes and recording the sensor's chronoamperometric response (after a quiet time of 10 s) while ACET actuation remained on. To characterize the response time of the amperometric sensor, the response time was defined as the time taken for the absolute gradient of current signal ($|\mathrm{d}i(t)/\mathrm{d}t|$), normalized with respect to the absolute signal value ($|i(t)|$), to fall below a given decay rate ε (here, selected as 2% per second), following the expression below [29]:

$$T_R = \min\left\{t : \left|\frac{1}{i(t)} \cdot \frac{\mathrm{d}i(t)}{\mathrm{d}t}\right| < \varepsilon\right\}$$

On-body ACET actuation-assisted sweat analysis

Sweat secretion stimulation was performed (following standard iontophoresis protocol, [27]) in two subjects during 12-h fasting and 0.5 h after glucose intake (30 g). For each case, the secreted sweat samples were interfaced with the microfluidic module, containing ACET actuation electrodes and glucose-enzymatic functionalized electrodes. The amperometric analysis was performed in the presence of ACET actuation (3.5 V_{RMS}).

Institutional Review Board (IRB) approval for human subject testing

The conducted human subject experiments were performed in compliance with the protocols that have been approved by the IRB at the University of California, Los Angeles (IRB#17-000170). All subjects gave written informed consent before participation in the study.

Results and discussion

CAD-to-3D microfluidic device fabrication and integration

Unlike conventional soft lithography PDMS-based microfluidic devices, which require resource-intensive cleanroom procedures and photomasks (with fixed designs) to create the master mold, laser-cutting involves only two simple steps: 1) designing the microfluidic layers of the device using a computer-aided design (CAD) software and 2) laser-cutting the loaded substrates (tape- or PET-based) to pattern the designed microfluidic features on a sequence of layers (Fig. 1a). The whole procedure typically takes on the order of a few minutes, which is significantly faster than soft lithography that takes on the order of at least a few hours. After laser-cutting the microfluidic layers, the device is assembled by sequentially and vertically stacking the layers (Fig 1b). The laser-cut 2D embodiments within the tape- and PET-based layers (optionally, pre-patterned with electrodes) form microchannels and VIAs. Scanning electron microscope (SEM) and optical microscope images of the top and cross-section view of a representative laser cut tape based microchannel are shown in Supplementary Fig. 1. With proper alignment (Supplementary Fig. 2) of VIAs and microchannels (Fig. 1c), fluidic connections in the vertical direction were achieved, rendering complex and spatially efficient 3D microfluidic structures. For example, as shown in Fig. 1d, the VIAs were designed to connect microfluidic pathways in different layers. Specifically, as shown in Fig. 1e, the red-dyed biofluid in the U-shaped channel weaved over and under the blue-dyed biofluid in the C-shaped channel while keeping the two liquids physically isolated. To validate the ability of our scheme to render well-sealed 3D microfluidic devices, an example microfluidic configuration is fabricated (with an interwoven over/under-pass design) and filled with color dyes. As can be seen in Fig. 1e, no leakage was found during the characterization period of > 72 hours. The flexible and the adhesive nature of the rendered microfluidic devices

allow for their ease of mating/integration with different types of surfaces, including curved glass, flexible printed circuit board (PCB), and human skin (Fig. 1f). To demonstrate the robustness of the microfluidic device adhesion to the body, first, an illustrative microfluidic device (composed of PET, double-sided tape, and skin adhesive medical tape) was adhered onto various body parts such as the forearm, thumb metacarpal, and thumb knuckle (with bending angles ranging from 18° to 108°, Supplementary Fig. 3a-c). Next, compression and twisting tests on the body-worn device indicated the preservation of the device's structural integrity and skin adhesion (no delamination) after application of external forces (Supplementary Fig. 3d-f). Lastly, the adhesion forces between multiple material interfaces were characterized using 180° peeling adhesion force characterization setup (Supplementary Fig. 3g, h). As shown in Supplementary Fig. 3i, the results indicate that the adhesion forces between all device internal layers are all significantly stronger than the adhesion force between skin and skin adhesive medical tape (which is commonly used in the reported literature and for medical use).

The devised fabrication and integration scheme can be adapted to implement a diverse set of bioanalytical operations. To inform the utility of our fabrication scheme, we demonstrated three example devices, as described below.
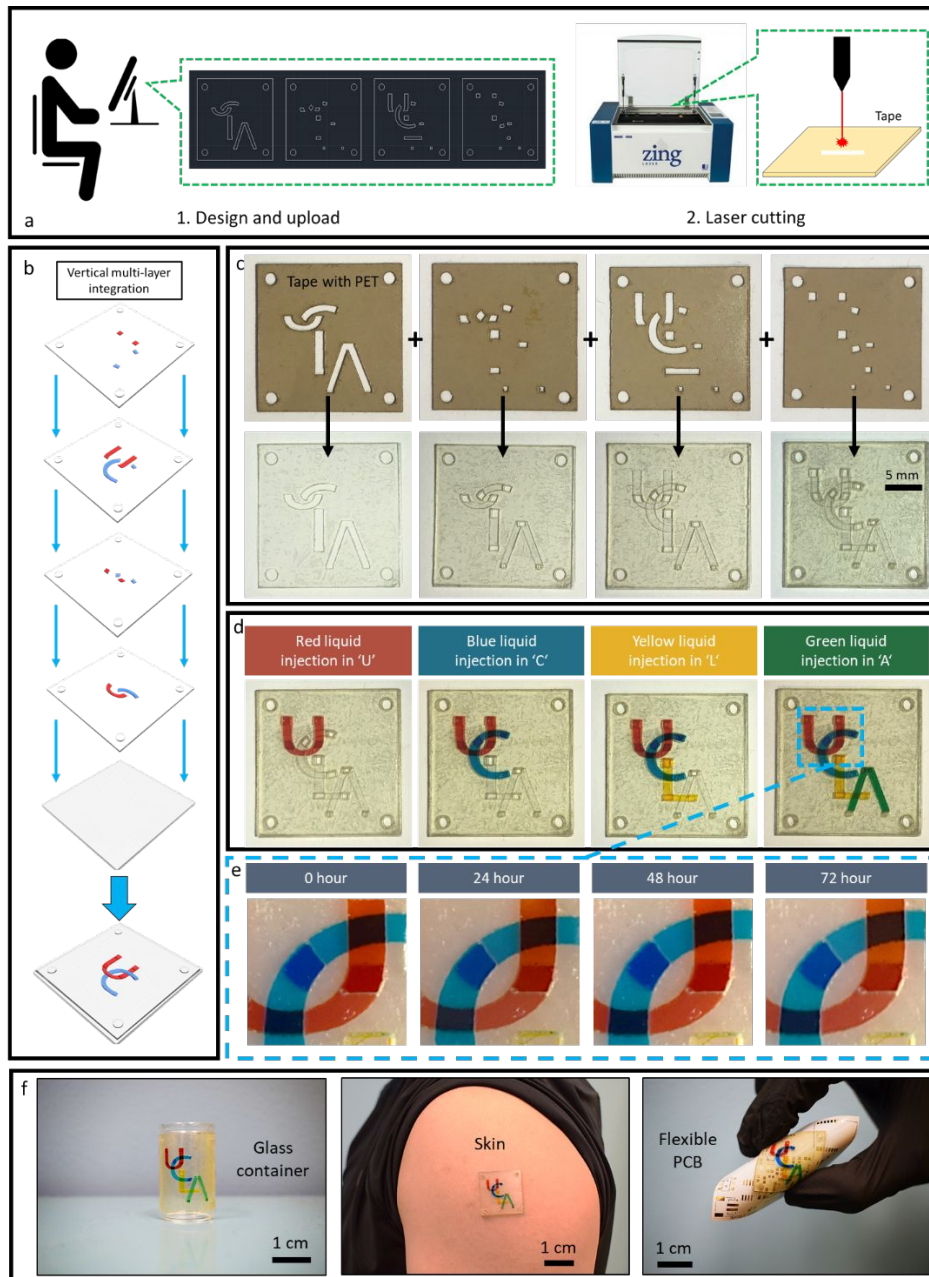
Figure 1. Overview of the CAD-to-3D flexible and adhesive microfluidic device fabrication and integration scheme: a) Conceptualized two-step fabrication of the microfluidic layers; b) Vertical assembly of the laser-cut microfluidic layers; c) Assembly of a representative 3D flexible and adhesive microfluidic device; d) Red-, Blue-, Yellow-, and Green- dyed artificial sweat samples are injected in U-, C-, L-, and A-shaped microfluidic channels to visualize the 3D integrated microfluidic module; e) Top-view and magnified images of the interwoven microfluidic region of the device, performed over 72 hours, illustrating that no leakage has occurred; f) Device mating/integration with curved glass, human skin, and flexible PCB.

Wearable microfluidic sweat sampling

A sweat collector for on-body application is designed with the Archimedean Spiral shape. As shown in Fig. 2a, the on-body collector is composed of two fluid layers: 1) the sweat collection chamber with the double-sided tape wall, PET ceiling, and the skin treated as substrate, and 2) the sweat flow channel with the double-sided tape wall and PET as both substrate and ceiling. In order to minimize the sample volume wasted in the chamber layer, a spacer layer (Scotch single sided self-seal laminating sheets, 3M, USA) was added to occupy liquid space in the chamber (reducing the dead volume to 1.7 $\mu L/cm^2$). Blue dye was embedded into the spiral channel layer during device assembly for visualization of the sweat sampling and progression. In comparison to the commercialized sweat collector (Fig. 2b), the designed collector is smaller, lighter, fully flexible (without any rigid part), and can stay attached to the skin as a standalone unit (sweat collection steps are shown in Supplementary Fig. 4).

To validate the robustness of sweat sampling on-body, the sweat collector was placed on an iontophoretically-stimulated area of the volar surface of the forearm of human subjects (two subjects, following standard iontophoresis protocol for sweat gland stimulation [27]). Figure 2c demonstrates our device's capability to reliably harvest sweat (no leakage in any of the composed layers) and to visualize the secretion process. To obtain the sweat secretion rate information, the secreted volume can be optically tracked by image analysis (detailed in the method section). Accordingly, sweat rate can be derived by calculating the slope of the sweat volume *vs.* time plot. As shown in Fig. 3d, for both subjects, the sweat secretion began at a maximal constant rate, followed by a decreasing trend with time.
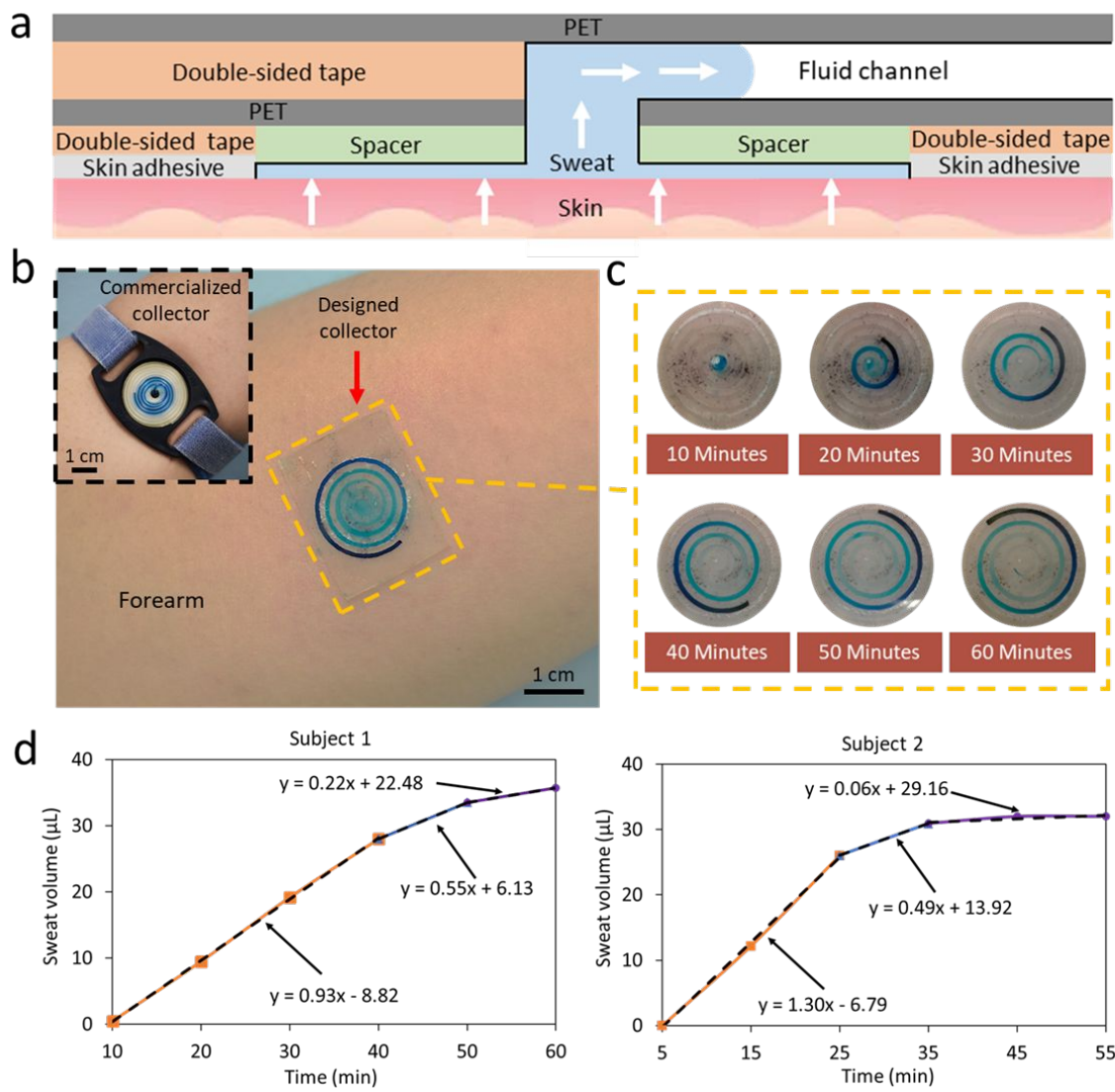
Figure 2. Wearable microfluidic sweat collector: a) Cross-section of the tape-based sweat collector structure; b) On-body application of the collector for sweat sampling, as a standalone unit. Inset shows the commercialized sweat collection device (Macroduct, ELITechGroup, France), which requires straps for holding down the device; c) Sequential optical images of the sweat secretion and *in-situ* collection in the designed sweat collector; d) Measured sweat volume *vs.* time profiles for two subjects (the sweat secretion rate is inferred from the slope of the curve-fitted lines at the desired time-points).

3D architecture for multi-step microscale filtration

Size-based filtration of microparticles (including cells or conjugated microbeads) allows for the implementation of a wide range of bioanalysis, by enabling sample processing operations

[26, 30, 31]. Here, we leverage the new degree of freedom achieved by the rendered 3D architectures to demonstrate filtering of microparticles. Accordingly, a flyover architecture, based on a network of over/under-pass microchannels, is implemented to perform multi-step size-based μ-scale filtration in z-axis, with the aid of vertically-integrated-filtration embodiments (incorporated during the device assembly). As shown in Fig. 3a, to realize the filtration embodiments, filter papers with pore sizes of 8 μm and 30 μm (Supplementary Fig. 5) are selectively embedded in the VIA structures.

To validate the filtration capability, an 80 μL buffer solution containing 2.2×10^3 beads/mL and 1.6×10^6 beads/mL concentrations of microbeads diameters 90 μm and 10 μm were introduced at the inlet. The sequential top-view images in Fig. 3b shows the progression of the introduced sample through all three microfluidic layers from the inlet to the outlet. The 90-μm and 10-μm beads were filtered out in two stages, specifically, upon passage through layer 1 to 2 (with filtration VIA pore size: 30 μm) and through layer 2 to 3 (with filtration VIA pore size: 8 μm). As can be seen from Fig. 3c, full bead filtration was achieved downstream of the 3D device.

The filtration results demonstrate the ability of the 3D structure to achieve operational complex microfluidic networks, while satisfying space-saving requirements for compact design. In the context of wearable biomarker sensing, μ-scale filtration may be adapted to eliminate the contamination arising from dead skin cells [23-25]. Additionally, this capability can be exploited to facilitate *in-situ* sample processing operations. For example, by incorporating microbeads, which are conjugated with surface markers, undesired analytes within the sample (*e.g.*, high concentration and interfering proteins) can be captured and subsequently get filtered using the demonstrated μ-scale filtration capability [26].
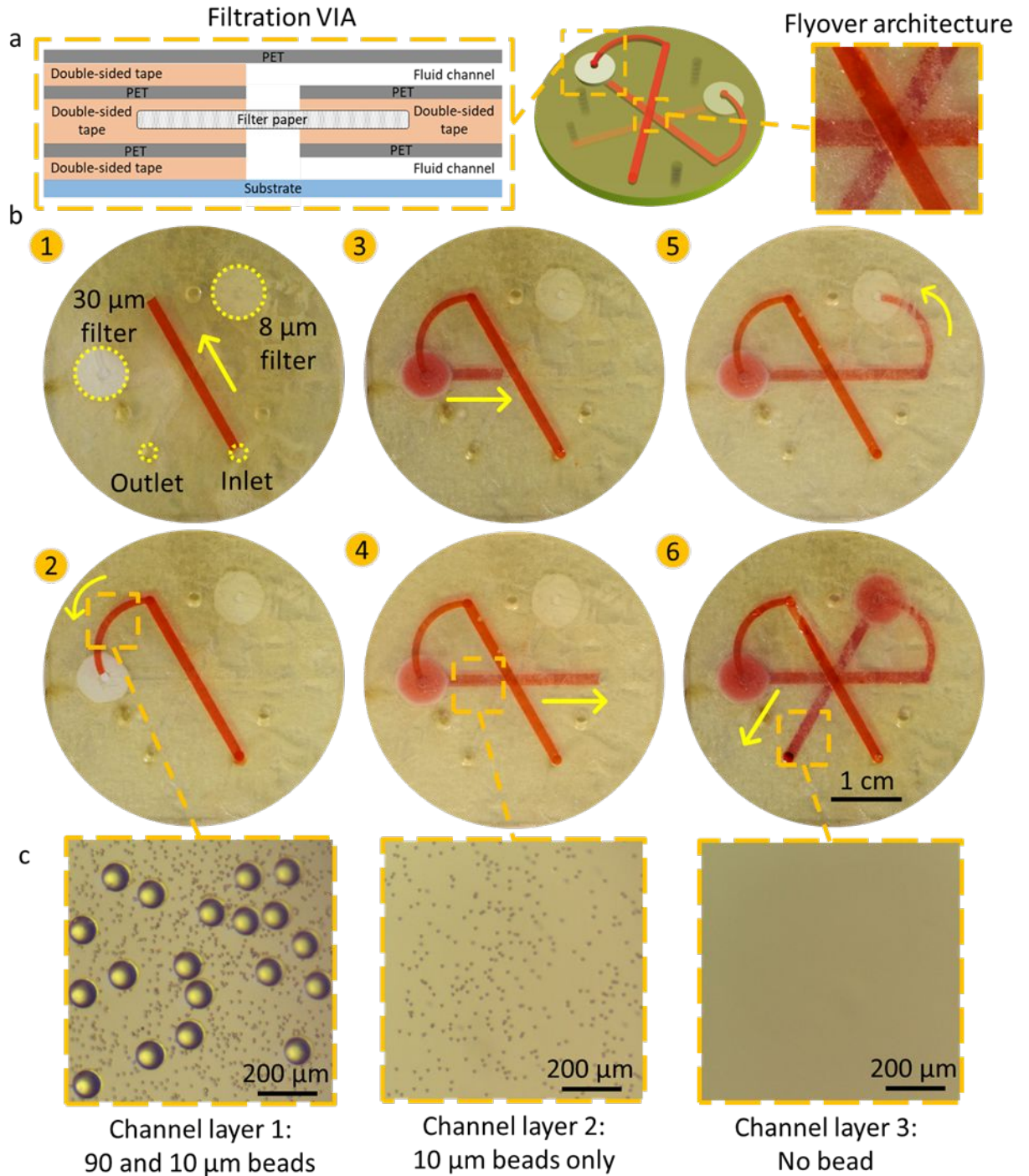
Figure 3: 3D and multi-step microscale filtration device: a) 3D and cross-section schematic of the filtration device structure, and the magnified optical image of the device's center; b) Sequential optical images of the injected fluid flow in the filtration device; c) Sequential microscopic images of upstream, midstream, and downstream of the device.

Sandwiched-electrode arrays for simultaneous biofluid actuation and sensing

The ability to fabricate multi-layered architectures was adapted to create a sandwiched-like actuation and sensing interface to further illustrate the value of the devised scheme in terms of enabling new degrees of freedom for device operation. To this end, we leveraged the vertical assembly approach, and incorporated electrode-patterned layers, which were aligned to face each other in order to realize a sandwiched-like interface, while forming the microfluidic channel (Fig. 4a). We specifically exploited this interface to demonstrate simultaneous ACET (with electrode pair on the ceiling) and electrochemical analysis (specifically, amperometric-based, with pre-functionalized electrode array on the bottom). The individual ACET and sensing electrode arrays, as well as the final assembled device are illustrated in Fig. 4b.

The design of the ACET electrode pair is based on a coplanar rotationally symmetric configuration [32]. The coplanar ACET electrode configuration allows for establishing a non-uniform electric field vector, which results in non-uniform joule heating and temperature gradient, and subsequently permittivity and conductivity gradients in the microfluidic channel. The interaction of the electric field with these gradient profiles results in body force acting on fluid, which in turn induces fluid motion [33,34]. Following the previously described approach [35], we simulated the ACET behavior of the actuation electrode pair. Figure 4c shows the corresponding simulated temperature profile as well as the induced micro-vortex-like flow pattern.

For electrochemical sensing, here, we specifically employed amperometric method (Fig. 4d-g), which is widely used for wearable enzymatic sensing (sensor development is described in the Materials and method section). First, we specifically characterized the effect of ACET actuation on H_2O_2 sensor amperometric response. Characterizing H_2O_2 sensing interface was motivated by the fact that H_2O_2 generation (proportional to the target concentration) is the last

reaction step involved in a large group of enzymatic sensing mechanisms (specifically, oxidase-based). The calibration curve of the ACET actuation-assisted H_2O_2 sensor (with 3.5 V_{RMS} applied across ACET electrode pair) was obtained and compared to the corresponding calibration curve where ACET actuation was not activated (a representative H_2O_2 sensor response is shown in Fig. 4d, steady-state response shown in Supplementary Fig. 6, reproduced results for two other sensors shown in Supplementary Fig. 7). Collectively, the results indicate that the activation of the ACET electrodes resulted in the 47 % and 26% enhancement in the H_2O_2 sensor output current level and sensitivity (defined as the slope of output current *vs.* analyte concentration, Fig. 4f), respectively. Furthermore, as illustrated in Fig. 4g the H_2O_2 sensor response time is reduced by 27% when the ACET actuation was activated (example annotated sensor response for time response determination is shown in Supplementary Fig. 8). In order to investigate this phenomenon in the context of enzymatic sensors, we studied the effect of ACET actuation on amperometric glucose sensor response, following the same characterization procedure (Fig. 4 e-g, Supplementary Fig. 6-8). Collectively, the same trends in the enhancement of the glucose sensor response was observed (74% and 31% increase in the output current level and sensitivity, respectively, and 33% reduction in the response time). To further validate the enhancement of the enzymatic sensor response in the presence of ACET actuation, we constructed and characterized a choline enzymatic sensor, where we observed the similar trends (Supplementary Fig. 9).

The enhancement in the sensor response can be attributed to both the effect of mixing (overcoming diffusion) as well as local temperature increase (*e.g.*, enhanced reaction rate at the sensor surface). Given that the improvement of the sensitivity and reduction of response time in both glucose and choline cases were on the same order of magnitude as those for the case of H_2O_2,

one may speculate that the acceleration of the H_2O_2 conversion and/or enhanced diffusion by ACET actuation plays a significant role in the sensor performance enhancement.

To validate the on-body operation of the devised actuation-assisted sensing interface, we performed human subject testing. Specifically, we demonstrated the elevation of sweat glucose after glucose intake in fasting subjects. Accordingly, standard iontophoresis protocol was followed for sweat stimulation of two healthy subjects during 12-h fasting and 0.5 h after consumption of 30 g of glucose. Upon each stimulation, the secreted sweat sample was interfaced with the ACET actuation-assisted glucose sensor (worn on body). As shown in Fig. 4h, the calibrated sweat sensor responses (measured in the presence of the ACET actuation, 3.5 V_{RMS}) for both subjects indicate the elevation of glucose level in sweat upon glucose intake, reflecting the elevation of glucose in blood.
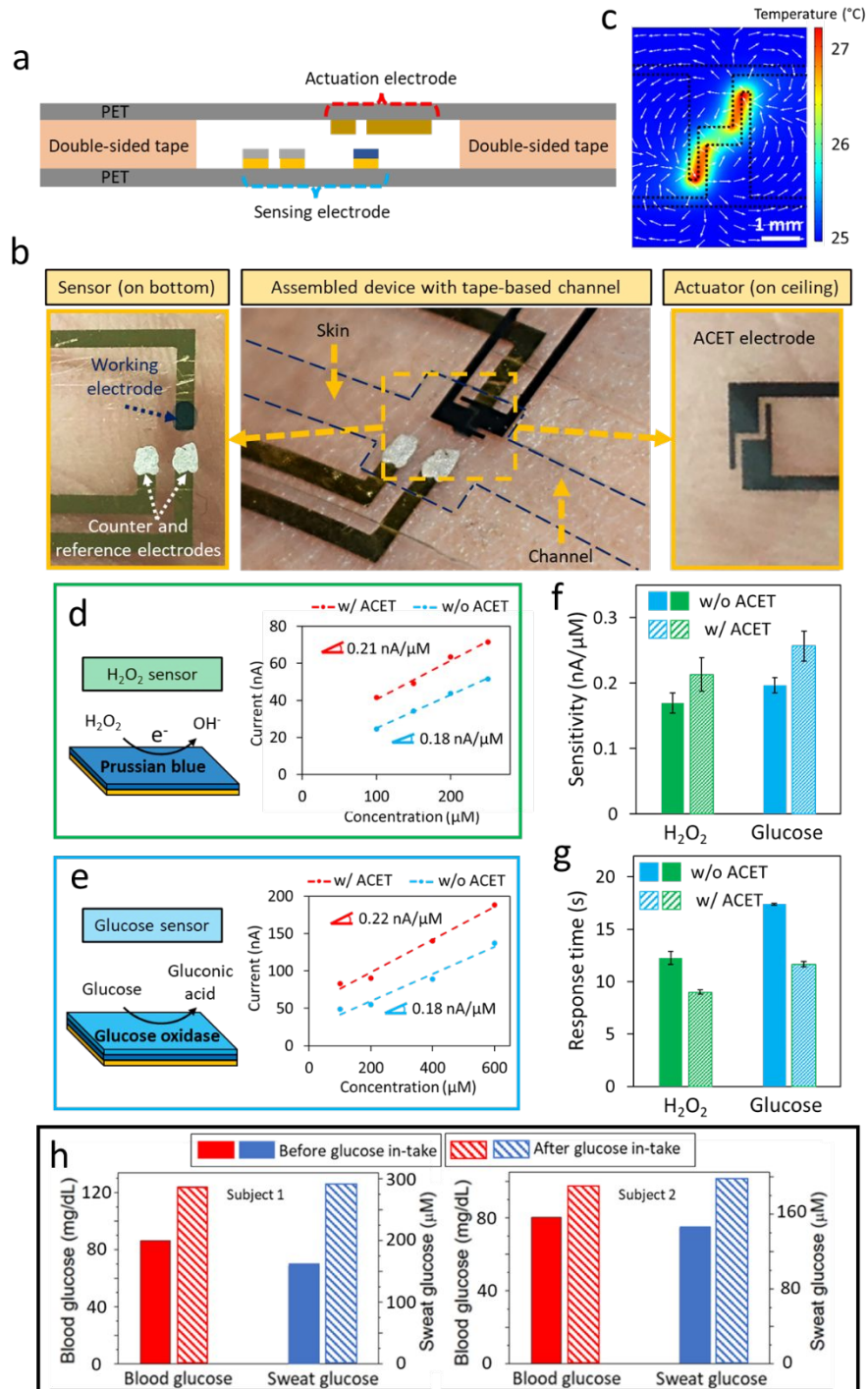
Figure 4: Sandwiched actuation and sensing interface: a) Cross-section schematic of the sandwiched-electrode array structure; b) Individual sensing (left) and actuation (right) electrode arrays, and final assembled device (middle, where the actuation electrode pair is aligned to face the sensor's working electrode). c) COMSOL ACET simulation (conductivity: 0.6 S/m, dielectric constant: 80, excitation: 3.5 V_{RMS}, ambient temperature: 25 °C), illustrating the temperature profile

and induced flow pattern established the rotationally symmetric electrode pair. d) Amperometric H_2O_2 sensing mechanism and corresponding calibration curves with and without ACET actuation. e) Enzymatic glucose sensing mechanism and corresponding calibration curves with and without ACET actuation. f, g) Comparison of corresponding amperometric sensors' sensitivities (f) and response time (g) with and without ACET actuation (error bars indicate standard error, N = 3). h) Comparison of blood and sweat glucose levels of two subjects during 12-h fasting and 0.5 h after glucose intake (30 g glucose), demonstrating the elevation of sweat glucose upon glucose intake, as measured by the actuation-assisted glucose sensor.

Conclusions

In conclusion, we devised a simple, scalable, and low-cost "CAD-to-3D Device" fabrication and integration scheme, which renders 3D and complex microfluidic architectures in a rapid manner. To inform the utility of our fabrication scheme, we demonstrated three example devices, to perform sweat collection (with visualizable secretion profile), sample filtration, and simultaneous biofluid actuation and sensing (using a sandwiched-like pair of electrode arrays). The spatial efficiency and new degrees of freedom achieved by the rendered 3D and multi-layered microfluidic architectures allows for the incorporation of a multitude of bioanalytical operations. The inherent simplicity of the devised scheme sets forth a feasible path for scalable and low-cost manufacturing of wearable microfluidic devices. In that regard, our scheme can be adapted for the fabrication and large-scale deployment of the currently reported and future bioanalytical wearable devices, which is critical at the prototyping level, for fueling large-scale clinical investigations, as well as at the production level for commercialized consumer applications and general population health monitoring.

Author contributions

H.L. and S.E. conceived the idea and designed the experiments; H.L. led the experiments (with assistance from Y.Z., S.L., X.C., Z.W., T.C., K.K., H.H., and S.E.); H.L., Y.Z., S.L., X.C., Z.W., T.C., W.Y., K.K., J.T., K.S., H.H., contributed analytic tools; H.L., Y.Z., S.L., B.W., C.Y., X.C., Z.W., W.Y., J.T., H.H., S.E. contributed to data analysis and interpretation; H.L., C.Y., S.L., Y.Z., B.W., K.K., H.H., and S.E. drafted the manuscript and all the authors provided feedback. S.E. supervised the study.

Conflicts of interest

There are no conflicts to declare.

Acknowledgements

References

1   J. Heikenfeld, A. Jajack, B. Feldman, S. W. Granger, S. Gaitonde, G. Begtrup and B. A. Katchman, *Nat. Biotechnol.*, 2019, **37**, 407–419.

2   J. Kim, A. S. Campbell, B. E.-F. de Ávila and J. Wang, *Nat. Biotechnol.*, 2019, **37**, 389–406.

3   Y. Yang and W. Gao, *Chem. Soc. Rev.*, 2019, **48**, 1465–1491.

4   M. Bariya, H. Y. Y. Nyein and A. Javey, *Nature Electronics*, 2018, 1, 160–171.

5   J. Kim, A. S. Campbell and J. Wang, *Talanta*, 2018, **177**, 163–170.

6   J. Heikenfeld, A. Jajack, J. Rogers, P. Gutruf, L. Tian, T. Pan, R. Li, M. Khine, J. Kim, J. Wang and J. Kim, *Lab Chip*, 2018, **18**, 217–248.

7   W. Gao, S. Emaminejad, H. Y. Y. Nyein, S. Challa, K. Chen, A. Peck, H. M. Fahad, H. Ota, H. Shiraki, D. Kiriya, D.-H. Lien, G. A. Brooks, R. W. Davis and A. Javey, *Nature*, 2016, **529**, 509–514.

8   S. Emaminejad, W. Gao, E. Wu, Z. A. Davies, H. Yin Yin Nyein, S. Challa, S. P. Ryan, H. M. Fahad, K. Chen, Z. Shahpar, S. Talebi, C. Milla, A. Javey and R. W. Davis, *Proc. Natl. Acad. Sci. U. S. A.*, 2017, **114**, 4625–4630.

9   A. Martín, J. Kim, J. F. Kurniawan, J. R. Sempionatto, J. R. Moreto, G. Tang, A. S. Campbell, A. Shin, M. Y. Lee, X. Liu and J. Wang, *ACS Sens*, 2017, **2**, 1860–1868.

10   X. Zhang, Y. Jing, Q. Zhai, Y. Yu, H. Xing, J. Li and E. Wang, *Anal. Chem.*, 2018, **90**, 11780–11784.

11   J. Choi, A. J. Bandodkar, J. T. Reeder, T. R. Ray, A. Turnquist, S. B. Kim, N. Nyberg, A. Hourlier-Fargette, J. B. Model, A. J. Aranyosi, S. Xu, R. Ghaffari and J. A. Rogers, *ACS Sens*, 2019, **4**, 379–388.

12   Y. Zhang, H. Guo, S. B. Kim, Y. Wu, D. Ostojich, S. H. Park, X. Wang, Z. Weng, R. Li, A. J. Bandodkar, Y. Sekine, J. Choi, S. Xu, S. Quaggin, R. Ghaffari and J. A. Rogers, *Lab Chip*, 2019, **19**, 1545–1555.

13   Y. Sekine, S. B. Kim, Y. Zhang, A. J. Bandodkar, S. Xu, J. Choi, M. Irie, T. R. Ray, P. Kohli, N. Kozai, T. Sugita, Y. Wu, K. Lee, K.-T. Lee, R. Ghaffari and J. A. Rogers, *Lab Chip*, 2018, **18**, 2178–2186.

14   X. He, T. Xu, Z. Gu, W. Gao, L.-P. Xu, T. Pan and X. Zhang, *Anal. Chem.*, 2019, **91**, 4296–4300.

15   A. Koh, D. Kang, Y. Xue, S. Lee, R. M. Pielak, J. Kim, T. Hwang, S. Min, A. Banks, P. Bastien, M. C. Manco, L. Wang, K. R. Ammann, K.-I. Jang, P. Won, S. Han, R. Ghaffari, U. Paik, M. J. Slepian, G. Balooch, Y. Huang and J. A. Rogers, *Sci. Transl. Med.*, 2016, **8**, 366ra165.

16   J. Choi, Y. Xue, W. Xia, T. R. Ray, J. T. Reeder, A. J. Bandodkar, D. Kang, S. Xu, Y. Huang and J. A. Rogers, *Lab Chip*, 2017, **17**, 2572–2580.

17   S. B. Kim, Y. Zhang, S. M. Won, A. J. Bandodkar, Y. Sekine, Y. Xue, J. Koo, S. W. Harshman, J. A. Martin, J. M. Park, T. R. Ray, K. E. Crawford, K.-T. Lee, J. Choi, R. L. Pitsch, C. C. Grigsby, A. J. Strang, Y.-Y. Chen, S. Xu, J. Kim, A. Koh, J. S. Ha, Y. Huang, S. W. Kim and J. A. Rogers, *Small*, 2018, **14**, e1703334.

18   P. Nath, D. Fung, Y. A. Kunde, A. Zeytun, B. Branch and G. Goddard, *Lab Chip*, 2010, **10**, 2286–2291.

19   D. I. Walsh 3rd, D. S. Kong, S. K. Murthy and P. A. Carr, *Trends Biotechnol.*, 2017, **35**, 383–392.

20   A. Kundu, T. Ausaf and S. Rajaraman, *Micromachines*, 2018, 9, 85.

21 D. C. Duffy, J. C. McDonald, O. J. Schueller and G. M. Whitesides, *Anal. Chem.*, 1998, **70**, 4974–4984.

22 D. Qin, Y. Xia and G. M. Whitesides, *Nat. Protoc.*, 2010, **5**, 491–502.

23 T. C. Boysen, S. Yanagawa, F. Sato and K. Sato, *J. Appl. Physiol.*, 1984, **56**, 1302–1307.

24 R. Peng, Z. Sonner, A. Hauke, E. Wilder, J. Kasting, T. Gaillard, D. Swaille, F. Sherman, X. Mao, J. Hagen, R. Murdock and J. Heikenfeld, *Lab on a Chip*, 2016, 16, 4415–4423.

25 J. Heikenfeld, *Electroanalysis*, 2016, 28, 1242–1249.

26 M. Javanmard, S. Emaminejad, C. Gupta, J. Provine, R. W. Davis and R. T. Howe, *Sens. Actuators B Chem.*, 2014, **193**, 918–924.

27 [anonymus Ac06619969], *Sweat Testing: Sample Collection and Quantitative Analysis, Approved Guideline*, 2000.

28 G. Matzeu, C. Fay, A. Vaillant, S. Coyle and D. Diamond, *IEEE Trans. Biomed. Eng.*, 2016, **63**, 1672–1680.

29 R. Baronas, F. Ivanauskas and J. Kulys, *Sensors*, 2003, 3, 248–262.

30 Y. Yoon, S. Kim, J. Lee, J. Choi, R.-K. Kim, S.-J. Lee, O. Sul and S.-B. Lee, *Sci. Rep.*, 2016, **6**, 26531.

31 Y. Cheng, X. Ye, Z. Ma, S. Xie and W. Wang, *Biomicrofluidics*, 2016, **10**, 014118.

32 S.-H. Huang, S.-K. Wang, H. S. Khoo and F.-G. Tseng, *TRANSDUCERS 2007 - 2007 International Solid-State Sensors, Actuators and Microsystems Conference*, 2007.

33 Y. Lu, T. Liu, A. C. Lamanda, M. L. Y. Sin, V. Gau, J. C. Liao and P. K. Wong, *J. Lab. Autom.*, 2015, **20**, 611–620.

34 J. Wu, M. Lian and K. Yang, *Applied Physics Letters*, 2007, 90, 234103.

35 H. C. Feldman, M. Sigurdson and C. D. Meinhart, *Lab Chip*, 2007, **7**, 1553–1559.